Actin-dependent vacuolar occupancy of the cell determines auxin-induced growth repression

David Scheuring[a], Christian Löfke[a], Falco Krüger[b], Maike Kittelmann[c], Ahmed Eisa[a], Louise Hughes[c], Richard S. Smith[d], Chris Hawes[c], Karin Schumacher[b], and Jürgen Kleine-Vehn[a,1]

[a]Department of Applied Genetics and Cell Biology, University of Natural Resources and Life Sciences, 1190 Vienna, Austria; [b]Center for Organismal Studies, University of Heidelberg, 69120 Heidelberg, Germany; [c]Department of Biological and Medical Sciences, Oxford Brookes University, Oxford OX3 0BP, United Kingdom; and [d]Department of Comparative Development and Genetics, Max Planck Institute for Plant Breeding Research, 50829 Cologne, Germany

Edited by Natasha V. Raikhel, Center for Plant Cell Biology, Riverside, CA, and approved November 30, 2015 (received for review September 1, 2015)

The cytoskeleton is an early attribute of cellular life, and its main components are composed of conserved proteins. The actin cytoskeleton has a direct impact on the control of cell size in animal cells, but its mechanistic contribution to cellular growth in plants remains largely elusive. Here, we reveal a role of actin in regulating cell size in plants. The actin cytoskeleton shows proximity to vacuoles, and the phytohormone auxin not only controls the organization of actin filaments but also impacts vacuolar morphogenesis in an actin-dependent manner. Pharmacological and genetic interference with the actin–myosin system abolishes the effect of auxin on vacuoles and thus disrupts its negative influence on cellular growth. SEM-based 3D nanometer-resolution imaging of the vacuoles revealed that auxin controls the constriction and luminal size of the vacuole. We show that this actin-dependent mechanism controls the relative vacuolar occupancy of the cell, thus suggesting an unanticipated mechanism for cytosol homeostasis during cellular growth.

auxin | vacuole | actin cytoskeleton | cell growth

Actin filaments and its myosin motor proteins control a multitude of diverse cellular processes in animal cells, such as muscle contraction, cell motility, as well as vesicle and organelle movements (1). In animals, actin has a strong impact on the regulation of cellular shape and thus on cell size (2). Unlike animal cells, plant cells are sheathed by shape-giving cell walls, rendering them largely immobile. Despite this difference, the plant actin cytoskeleton has a conserved function in vesicle trafficking and organelle movement (3). Compared with animals, the role of actin in controlling cell size in plants is not clear and remains to be addressed. The phytohormone auxin is a crucial regulator of cell-size control in plants (4). Several studies suggest that the plant-specific growth regulator auxin affects the actin cytoskeleton (5–10). These studies concentrated on the effect of auxin on cortical actin and its contribution to processes close to the plasma membrane, such as endocytosis and exocytosis (5–11). Here we show that the actin cytoskeleton also is required for auxin processes beyond the plasma membrane, contributing to vacuolar morphogenesis and consequently to the regulation of cell size in plants.

Results and Discussion

To assess the organization of actin filaments in root epidermal cells, we used the actin marker Lifeact–Venus [a 17-amino acid peptide fused to Venus, which stains filamentous (F-) actin structures (12)] and measured the density of actin in cortical sections of late meristematic cells. The exogenous application of auxin [naphthaleneacetic acid (NAA); 500 nM, 6 h) led to a higher fluorescent intensity of Lifeact–Venus (Fig. S1 *A–F*) and significantly increased the integrated density of actin filaments (Fig. 1 *A–C*). This increase was sensitive to auxinole (13), a designated inhibitor of Transport Inhibitor Response 1 (TIR1)/Auxin Signaling F-Box (AFB) auxin receptors (Fig. S1 *G–L*).To define further the actin filament organization beyond the cell cortex, we used gated stimulated emission depletion (gSTED) superresolution live-cell imaging and performed defined z-stack imaging on epidermal root cells. Application of auxin (250 nM, 20 h) increased the skewness of actin filaments in maximum projections (Fig. 1 *D–F*), suggesting a higher degree of actin filament bundling (14) in entire cells. Our data suggest that auxin signaling also influences actin-dependent processes beyond the plasma membrane, leading to a tighter network of actin filaments.

We recently reported that auxin controls the morphogenesis of the largest plant organelle, the vacuole in a TIR1/AFBs-dependent manner that is required for auxin-induced growth repression (15). Using confocal microscopy, we detected the actin cytoskeleton in the vicinity of the vacuole (Fig. S2); this observation is consistent with the proteomic detection of actin at isolated vacuoles (16, 17). Interference with actin affects the formation of transvacuolar strands (18, 19), raising the question of whether the actin network is mechanistically linked to vacuolar morphogenesis required for auxin-reliant growth repression. To assess the role of actin in the vacuolar morphology of epidermal root cells, we first interfered with actin dynamics pharmacologically. Depolymerization of actin by Latrunculin B (LatB) induced roundish vacuolar structures (Fig. S3 *A*, *B*, *E*, and *F*). LatB treatment also reduced the size (width × length) of the largest luminal structure, which defines the vacuolar morphology index (Fig. S3*D*) (15). Similarly, Jasplakinolide (JASP)-dependent stabilization of actin affected the vacuolar shape and increased the vacuolar morphology index (Fig. S3 *A*, *C–E*, and *G*). Notably, the effect of JASP on vacuoles was most pronounced in cells shortly before elongation. In contrast to actin, microtubules were not enriched in the vicinity of the tonoplast (Fig. S2 *B* and *C*), and oryzalin-induced depolymerization

Significance

Control of cell size is fundamentally different in animals and plants. The actin cytoskeleton has a direct impact on the control of cell size in animals, but its mechanistic contribution to cellular growth in plants remains largely elusive. Here, we show that actin is used in a plant-specific growth mechanism by controlling the volume of the largest plant organelle, the vacuole. Actin is required for the auxin-dependent convolution and deconvolution of the vacuole, steering the vacuolar occupancy of the cell. This function indirectly impacts cytosol size and presumably allows plant cells to grow without alterations in cytosolic content. These findings could lead to a better understanding of plant cells' ability to expand faster than vacuole-lacking animal cells.

Author contributions: D.S., C.L., F.K., M.K., R.S.S., C.H., K.S., and J.K.-V. designed research; D.S., C.L., F.K., M.K., A.E., L.H., and C.H. performed research; D.S., C.L., F.K., M.K., R.S.S., C.H., and J.K.-V. analyzed data; and D.S. and J.K.-V. wrote the paper.

The authors declare no conflict of interest.

This article is a PNAS Direct Submission.

Freely available online through the PNAS open access option.

[1]To whom correspondence should be addressed. Email: juergen.kleine-vehn@boku.ac.at.

This article contains supporting information online at www.pnas.org/lookup/suppl/doi:10.1073/pnas.1517445113/-/DCSupplemental.

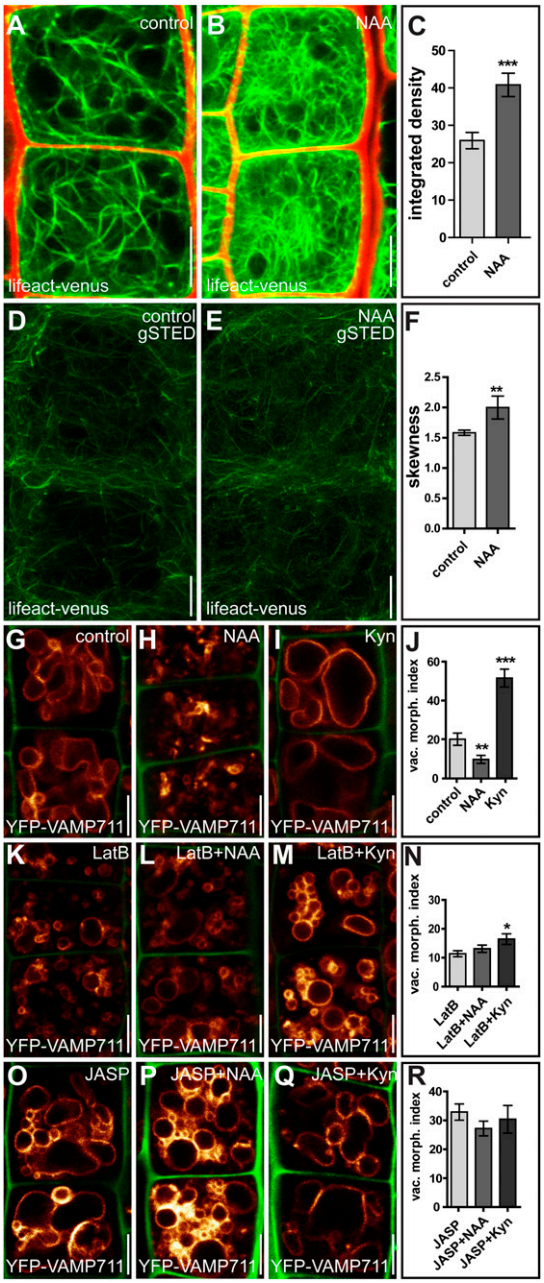

Fig. 1. Auxin impacts the actin cytoskeleton and actin-dependent vacuolar morphology. (*A*–*C*) Measurements of the integrated density of actin filaments (Lifeact–Venus) in cortical sections of root epidermal cells. (*A*) Cells treated with DMSO (control). (*B*) Cells treated with auxin (NAA; 500 nM, 6 h). (*C*) Quantification of the integrated density of actin filaments. ***$P < 0.001$. (*D* and *E*) gSTED superresolution microscopy of actin filaments of root epidermal cells treated with DMSO (control) (*D*) and auxin (NAA; 250 nM, 20 h) (*E*). (*F*) Quantification of the skewness of actin filament organization. **$P < 0.01$. (*G*–*I*) Control seedlings treated with DMSO (control) (*G*), auxin (NAA; 500 nM, 6 h) (*H*), or Kyn (2 μM, 6 h) (*I*). (*J*) The vacuolar morphology index (expressed in square micrometers) depicts the effects of auxin on vacuolar appearance. **$P < 0.01$, ***$P < 0.001$. (*K*–*M*) LatB (500 nM, 6 h) treatment led to more circular vacuolar structures (*K*) and imposed a reduced response to auxin (NAA) (*L*) and Kyn (*M*) treatment. (*N*) Quantification of the vacuolar morphology index. *$P < 0.05$. (*O*–*Q*) Treatment with JASP (2.5 μM, 6 h) led to distorted vacuolar structures (*O*), which imposed a partial resistance to auxin (NAA) (*P*) and Kyn (*Q*) cotreatment. (*R*) Quantification of the vacuolar morphology index. Data represent means ± SEM (n = 35–70 cells for *C*, 10 z-stacks for *F*, and 30 cells from six individual seedlings for *J*, *N*, and *R*). YFP-VAMP711 (orange) and PI (red for *A* and *B*, green for *G*–*Q*) were used to highlight the vacuole and the cell wall, respectively. (Scale bars: 5 μm.)

of microtubules had no immediate effect on vacuolar morphology (Fig. S4). Our findings suggest that interference with actin, not microtubule dynamics, affects the vacuolar morphology.

Based on these data, we assumed that the effect of auxin on actin also may impact vacuolar shape, and subsequently we investigated whether the actin cytoskeleton is required for the auxin-induced changes in vacuolar morphology. To do so, we induced high- and low-auxin conditions in the presence of actin-affecting drugs. Exogenous application of auxin leads to a significantly lower vacuolar morphology index in meristematic cells of the root epidermis (Fig. 1 *G*, *H*, and *J*) (15). We also depleted cellular auxin by applying the auxin biosynthesis inhibitor kynurenine (Kyn), which leads to a significantly higher vacuolar morphology index in wild-type cells (15) (Fig. 1 *G*, *I*, and *J*). In contrast, actin depolymerization and stabilization resulted in vacuoles that were less affected by auxin (Fig. 1 *K*, *L*, *N*–*P*, and *R*) and Kyn application (Fig. 1 *K*, *M*–*O*, *Q*, and *R*).

We accordingly conclude that pharmacological interference with actin abolishes auxin-induced changes in vacuolar morphology (Fig. 1 *G*–*R*) and suggest that the actin cytoskeleton is mandatory in instructing both smaller and larger luminal vacuoles. In support of this pharmacological approach, moderate genetic interference with actin and its motor protein myosin distinctly reduced the effect of auxin on vacuolar morphology. Actin mutants, such as *act7-4* (20) and *act2/act8* (21), as well as the myosin mutants *xi-k/1/2* and *xi-k/1/2/i* (22), showed subcellular resistance to auxin, displaying partially insensitive vacuoles (Fig. 2 *A*–*N*). This observation confirms that the actin–myosin system is required for the effect of auxin on vacuolar morphology.

As previously reported, control of vacuolar morphology is required for auxin-dependent growth repression (15). We therefore tested whether the subcellular resistance to auxin would also lead to auxin-resistant cellular elongation in actin and myosin mutants. We consequently recorded the maximum expansion of root epidermal cells in the elongation zone of untreated and auxin-treated seedlings. Auxin treatment (125 nM, 20 h) inhibited expansion in wild-type root epidermal cells (Fig. 2 *O*, *P*, and *U*), but genetic interference with actin and myosin induced a partial resistance to auxin (Fig. 2 *Q*–*U*). Notably, mild pharmacological interference with actin, by low doses of LatB (125 nM, 20 h), not affecting cellular elongation rates on its own, similarly blocked auxin-induced growth repression (Fig. 2*V* and Fig. S3 *H*–*K*). These data suggest that the actin cytoskeleton influences the auxin-dependent vacuolar morphology required for cellular growth control.

Auxin controls the abundance of vacuolar SNARE complex components, which are required for its effect on vacuolar morphology and cellular growth repression (15). The root growth of the vacuolar SNARE mutant *vti11* was less affected than that of wild-type plants when germinated on medium containing LatB (100 nM) (Fig. S5 *A* and *B*). This resistance could be caused by altered vacuolar morphogenesis, because the *vti11* vacuoles remained larger when treated with LatB (Fig. S5 *C*–*I*; compare *C* with *G*). Notably, pharmacological inhibition of PI3- and PI4-kinases by wortmannin (WM) (33 μM, 6 h) not only interferes with auxin-induced stability of SNAREs (15) but also abolishes the effect of auxin (500 nM, 6 h) on Lifeact–Venus density and abundance (Fig. S6 *A*–*J*). On the other hand, genetic and pharmacological interference with phosphatidylinositols strongly reduced the effect of LatB (500 nM, 6 h) and JASP (2.5 μM, 6 h) on vacuolar morphology (Fig. S6 *K*–*T*). Nevertheless, LatB and JASP treatments did not block auxin-induced stabilization of vacuolar SNARE YFP-VAMP711 (Fig. S7). Even though this interaction requires further in-depth investigation, this set of data suggests that actin- and SNARE-dependent processes have at least partially interdependent impacts on auxin-controlled vacuolar morphology.

We subsequently investigated the cellular mechanism by which the actin cytoskeleton affects vacuolar function. Auxin treatment

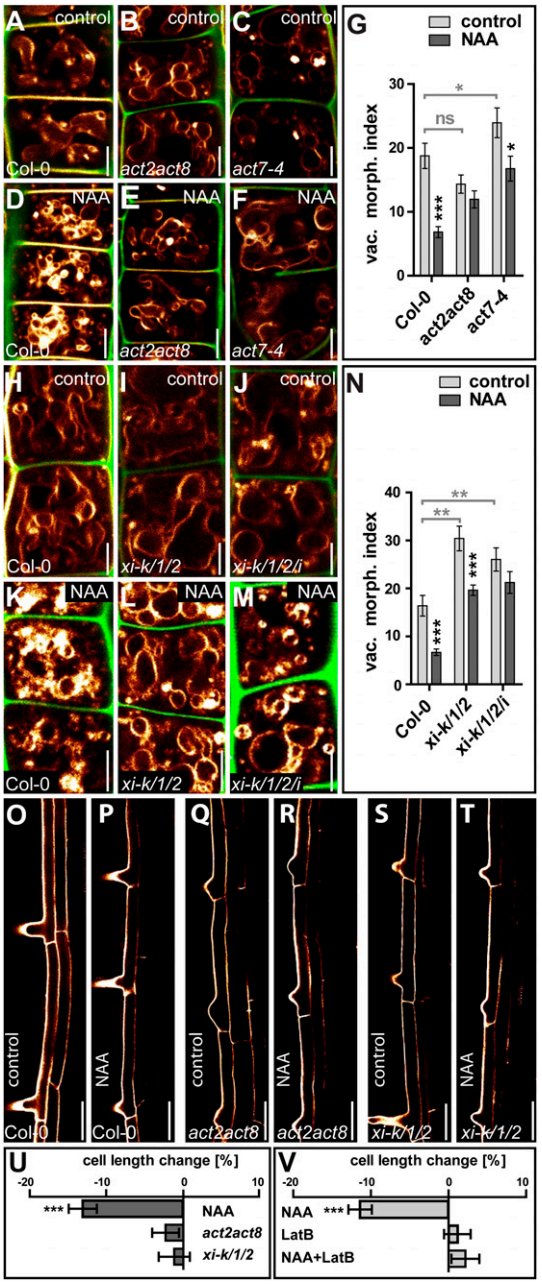

Fig. 2. Genetic interference with the actin–myosin system abolishes the effect of auxin on vacuolar morphology and cellular growth rates. (*A–C*) DMSO solvent treatment (control) of wild-type *Col-0* (*A*), the actin double-mutant *act2act8* (*B*), and the *act7-4* single mutant (*C*). (*D–F*) Auxin (NAA; 250 nM, 20 h) treatment of wild-type *Col-0* (*D*), *act2act8* (*E*), and *act7-4* (*F*) seedlings. (*G*) The vacuolar morphology index decreased strongly in control plants, but actin mutants were less affected by auxin. Light gray bars and asterisks indicate statistical evaluation based on untreated vacuoles. $*P < 0.05$, $***P < 0.001$. ns = not significant. (*H–J*) DMSO solvent treatment (control) of wild-type *Col-0* (*H*) and myosin triple (*xi-k/1/2*) (*I*) and quadruple (*xi-k/1/2/i*) (*J*) mutants. (*K–M*) Auxin treatment of wild-type *Col-0* (*K*), *xi-k/1/2* (*L*), and *xi-k/1/2/i* (*M*) seedlings. (*N*) Although the vacuolar morphology index decreased significantly in control plants, myosin mutants were only mildly affected by auxin. Light gray bars and asterisks indicate statistical evaluation based on untreated vacuoles. $**P < 0.01$, $***P < 0.001$. (*O–V*) Changes in cell length in fully elongated root cells in the differentiation zone. Compared to *Col-0* wild-type seedlings treated with DMSO (*O*), auxin (125 nM, 20 h) (*P*) treatment led to a reduction in cell length (*U*). Neither the *act2act8* (*Q* and *R*) nor *xi-k/1/2* (*S* and *T*) mutant seedlings showed a significant reduction in cell length upon auxin treatment (*U*). $***P < 0.001$. (*V*) Pharmacological interference with actin by LatB (125 nM; 20 h) similarly blocked auxin-induced growth repression. $***P < 0.001$. Data represent means ± SEM ($n = 30$ cells from six individual seedlings in *G* and *N* and $n = 35$ cells from nine individual roots in *U* and *V*). MDY-64 (orange) and PI (green for *A–M*, orange for *O–T*) were used to highlight the vacuole and the cell wall, respectively. (Scale bars: *A–F* and *H–M*, 5 μm; *O–T*, 50 μm.)

seemingly leads to the formation of multiple small luminal vacuoles (15), and several studies previously have addressed the mechanisms of vacuolar fragmentation (16, 18, 23–25). Accordingly, actin and its motor protein myosin could contribute the force required for auxin-dependent vacuolar fission and fusion events. Conversely, other studies have shown that several plant cells show interconnected vacuolar structures (26–31). Accordingly, the actin–myosin system could generate or release vacuolar constrictions. We therefore addressed whether auxin impacts either the fragmentation or the constriction of the vacuole.

We used serial block-face scanning electron microscopy (SBF-SEM) and 3D reconstruction to obtain a nanometer resolution of the epidermal cell vacuole. Untreated cells showed largely interconnected vacuolar cisternae (Fig. 3*A* and Movie S1). Similarly, auxin-treated samples showed interconnected structures, but the vacuolar cisternae appeared much smaller and more numerous (Fig. 3*B* and Movie S2). This finding suggests that auxin does not lead primarily to vacuolar fragmentation but rather to more constriction. To assess this finding quantitatively in living cells, we used fluorescent recovery after photo-bleaching (FRAP) (27) on the luminal vacuole dye BCECF [2′,7′-Bis-(2-Carboxyethyl)-5-(and-6)-Carboxyfluorescein] (32). After photo-bleaching, the luminal dye recovered readily in untreated epidermal cells (Fig. 3 *C–E* and *I*), confirming the mainly interconnected nature of the vacuole. Most vacuoles also showed FRAP in response to auxin, but the recovery was slower than that of untreated controls (Fig. 3 *F–I*). The slower recovery substantiates auxin-induced constrictions of interconnected vacuoles, leading to a reduced rate of luminal diffusion through tubular structures. Notably, an increased fraction of vacuoles did not show recovery in the analyzed time frame (Fig. S8 *A* and *B*), suggesting that auxin also increases the occurrence of solitary vacuoles. Nevertheless, this set of data strongly indicates that auxin does not lead primarily to vacuolar fragmentation, as initially implied by 2D imaging (Fig. 1*H*) (15), but rather to vacuolar constriction.

To unravel the importance of vacuolar constriction further, we used BCECF imaging to obtain a cellular view of the vacuolar volume. The increase in vacuole size during cellular expansion was visibly suppressed by the application of auxin (Fig. S9 *A* and *B*). Notably, auxin treatment strongly decreased the vacuolar volume and consequently shifted the vacuole surface-to-volume ratio in wild-type late meristematic epidermal cells (Fig. 4 *A–D* and Movies S3 and S4) but not after pharmacologic or genetic interference with actin/myosin (Fig. 4 *E–M*). The ensuing assumption—that auxin might define how much cell space a vacuole occupies—led us to use MorphoGraphX (33) to measure vacuolar volume in relation to the cell volume. Intriguingly, auxin treatment restricted the vacuolar occupancy of the cell (Fig. 4 *N*, *O*, and *V*), but the effect of auxin on vacuolar occupancy was abolished by pharmacological or genetic interference with actin/myosin dynamics (Fig. 4 *P–V*).We accordingly conclude that auxin negatively regulates the vacuolar volume in an actin-dependent manner, directly influencing the relative vacuolar occupancy of the cell.

Our work reveals that the actin cytoskeleton has a role in controlling cell size in plants. Actin operates in a plant-specific growth mechanism by controlling the volume of the largest plant organelle, the vacuole. Low and high auxin levels can expand and constrict the plant vacuole, respectively. Vacuolar SNAREs are involved in this process (15) and appear to interact with actin-dependent processes. Notably, several SNARE proteins seem to interact physically with actin (34), but whether such interaction affects vacuolar morphogenesis remains to be investigated. We

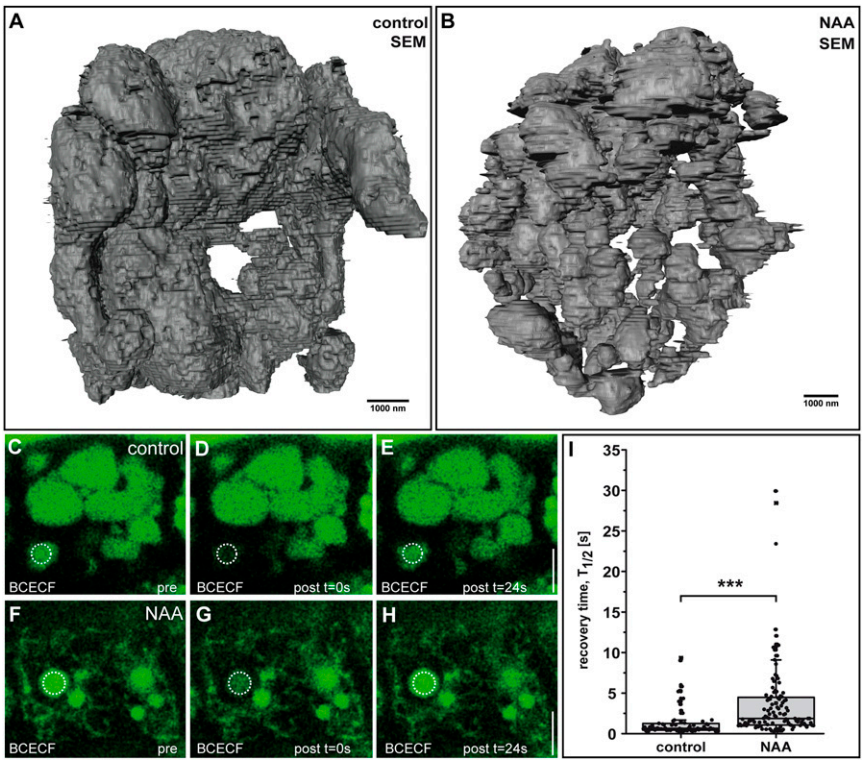

Fig. 3. Auxin induces vacuolar constrictions. (*A* and *B*) SEM-based rendering of vacuoles in *Arabidopsis* root epidermal cells treated with DMSO solvent (*A*) or auxin (NAA; 250 nM, 20 h) (*B*). (*C–H*) FRAP measurements of *Col-0* seedlings stained with BCECF-AM and treated with DMSO solvent (control) (*C–E*) or auxin (NAA; 250 nM, 18 h) (*F–H*). (*I*) The FRAP recovery time was significantly longer after auxin treatment than in untreated seedlings. ***$P < 0.001$. Data are represented as boxplots ($n = 70$ bleached structures for the control and $n = 112$ bleached structures for auxin treatment). (Scale bars: *A* and *B*, 1,000 nm; *C–H*, 5 μm.)

show that auxin induces tighter arrangements of actin filaments and thereby may physically restrict the expansion of vacuoles. However, we cannot rule out the possibility that actin-dependent vesicle transport also may contribute to vacuolar shapes. Actin and myosin mutants are partially resistant to auxin, presumably because of their inability to implement auxin-induced changes in the actin cytoskeleton. Rather unexpectedly, we report that in late meristematic cells of the root epidermis the vacuolar shape depends mainly on actin-dependent constrictions and not on homotypic fusions. Moreover, we have shown that actin indeed is required for the auxin-dependent cellular occupancy of the vacuole. It is conceivable that the vacuole has an important space-filling function during growth, and we hypothesize that this mechanism allows a plant cell to elongate without altering its cytosolic matter. This notion tallies with previous findings that the cytosolic content does not correlate with cell size in plant cell cultures (35). Accordingly, auxin would limit the intracellular expansion of the vacuole to restrict cellular growth potential.

In protists, the contractile vacuole regulates the quantity of water in a cell (36). It is possible that vacuoles maintain a related role in multicellular organisms, such as fungi, algae, and land plants. All these organisms show rapid cellular elongation rates by massive cellular uptake of water; such uptake possibly risks cytosol dilution. Although the movement of water and soluble material between the cytosol and vacuolar lumen remains to be addressed in our experimental setup, it is tempting to postulate that vacuole enlargement could compensate for this cellular flooding in a partially actin-dependent manner. Accordingly, we propose a model of cellular growth in which auxin restricts the vacuolar volume presumably required for cytosol homeostasis during cellular expansion.

Methods

Plant Materials and Growth Conditions. *Arabidopsis thaliana*, ecotype *Columbia 0* (*Col-0*) was used. The following plant lines were published previously: 35S::Lifeact–Venus (37), 35S::GFP-ABD2 (38, 39), 35S::MAP4-GFP (40), *act7-4* (20), *pUBQ10::YFP-VAMP711* (Wave 9Y/R) (41), *act2-1/act8-2* (21), *xi-k/1/2* and *xi-k/1/2/l* (22), *pi4kß1/2* (42), and *vti11* (43). Seeds were stratified at 4 °C for 2 d in the dark and were grown on vertically orientated 1/2 Murashige and Skoog (MS) medium plates under a long-day regime (16 h light/8 h dark) at 20–22 °C.

Chemicals. All chemicals were dissolved in DMSO and were applied in solid or liquid 1/2 MS medium. Dyes were applied in liquid 1/2 MS medium before imaging. NAA, 1-naphthaleneacetic acid (1-NAA), and 2-naphthaleneacetic acid (2-NAA) were obtained from Duchefa; FM4-64, Kyn, LatB, and propidium iodide (PI) were obtained from Sigma-Aldrich; and BCECF-AM, MDY-64, and JASP were obtained from Life Technologies. WM was obtained from Cayman Chemical Co., and auxinole was kindly provided by Ken-ichiro Hayashi, Okayama University of Science, Okayama, Japan (13).

Phenotype Analysis. For the quantification of vacuolar morphology and cell-length change, 7-d-old seedlings were used. To analyze the vacuolar morphology index, subcortical confocal sections (above the nucleus) of the root epidermis were acquired [according to Löfke et al. (15)] and were processed further with ImageJ software (rsb.info.nih.gov/ij/). Images were taken in the late meristematic zone, as described previously (15). For JASP treatments, cells were quantified shortly before the onset of elongation (below the transition zone). The largest luminal structures in at least five epidermal atrichoblast cells were quantified by measuring the longest and widest distance and were processed by multiplying the values [termed the "vacuolar morphology index" (15)]. Quantification of the final change in cell length in elongated epidermal root hair cells was carried out on median confocal sections. To estimate positions for cell length measurements in the elongation zone, seedlings were stained with PI (0.02 mg/mL) for 5 min, and images subsequently were acquired at points where no PI entered the vasculature, depicting differentiated endosomal diffusion barriers (15). The quantification of integrated density was carried out using cortical sections of root epidermal cells. Integrated density was determined using the respective analysis option in ImageJ. For measurements of signal intensity (mean gray value) of the actin cytoskeleton, a rectangle of 4,000 μm^2 was drawn in the meristematic zone of the root, and the mean gray value of 15–20 cells per condition was analyzed. For every treatment a minimum of 75 cells were considered. For analysis of the root length, seedlings grown on vertically orientated plates were scanned on a flat-bed scanner, and measurements were performed in ImageJ. In each condition, 15–20 seedlings were analyzed 8 d after germination for each experiment.

Confocal Microscopy. For live cell imaging, 6-d-old seedlings were used. For image acquisition a Leica SP5 (DM6000 CS), a TCS acousto-optical beam

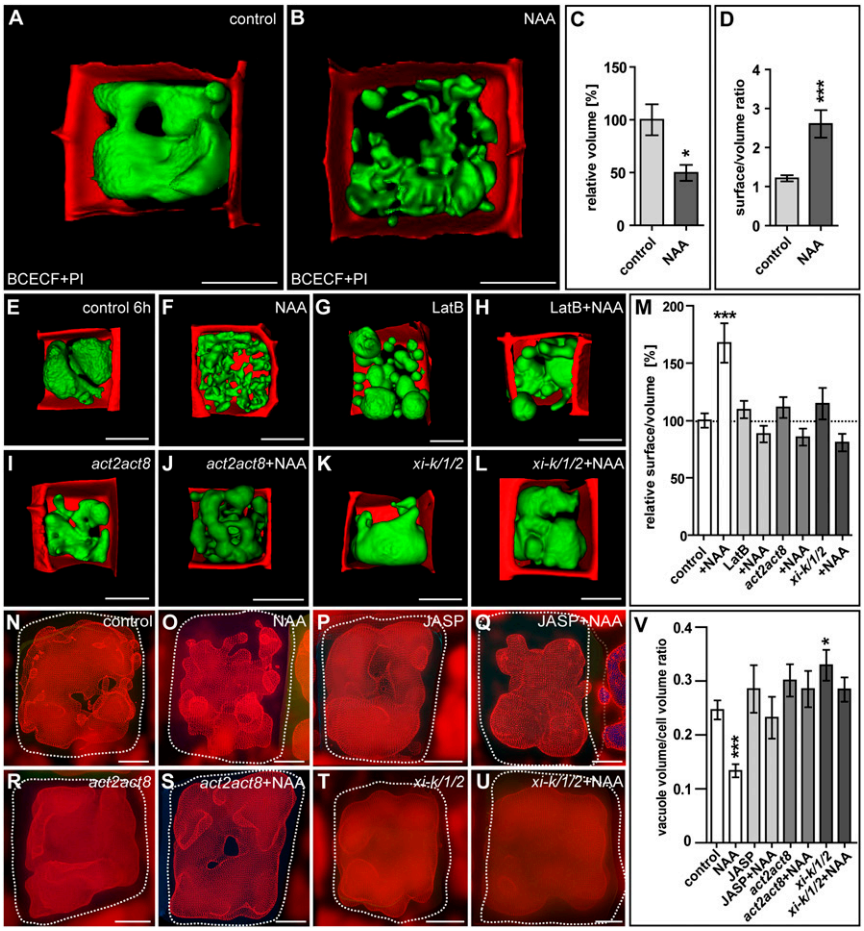

Fig. 4. Auxin controls the actin-dependent cellular occupancy of the vacuole. (*A* and *B*) Surface renderings of vacuoles of *Col-0* seedlings treated with DMSO (control) (*A*) or auxin (NAA; 250 nM, 20 h) (*B*). Seedlings were stained with BCECF-AM (green), and PI (red). (*C* and *D*) Quantification of relative vacuole volume (*$P < 0.05$) (*C*) and surface-to-volume ratio (***$P < 0.001$) (*D*) for control and auxin treatment. (*E–H*) Surface renderings of vacuoles after treatment with DMSO (control) (*E*), auxin (NAA; 500 nM, 6 h) (*F*), or LatB (500 nM, 6 h) (*G*) or cotreatment with LatB and auxin (*H*). (*I–L*) Surface renderings of DMSO-treated *act2act8* (*I*) and *xi-k/1/2* (*K*) mutants and auxin-treated *act2act8* (*J*) and *xi-k/1/2* (*L*) mutants. (*M*) Surface-to-volume ratios. ***$P < 0.001$. (*N–Q*) MorphoGraphX-based cellular and vacuolar segmentation to quantify volume in cells treated with DMSO (control) (*N*), auxin (NAA) (*O*), JASP (2.5 μM, 6 h) (*P*), or cotreated with JASP and NAA (*Q*). (*R–U*) Cellular and vacuolar segmentation of *act2act8* (*R* and *S*) and *xi-k/1/2* (*T* and *U*) mutants treated with DMSO (*R* and *T*) or with auxin (NAA) (*S* and *U*). (*V*) MorphoGraphX software was used to measure vacuolar volume in respect to cellular volume. *$P < 0.05$, ***$P < 0.001$. Data represent means ± SEM ($n = 10$ z-stacks from five individual seedlings for every condition for *C, D,* and *M* and $n > 11$ cells for *V*). (Scale bars: 5 μm.)

splitter confocal laser-scanning microscope was used, equipped with a Leica HC PL APO CS 20 × 0.70 IMM UV objective or a Leica HCX PL APO CS 63 × 1.20 water-immersion objective. MDY-64 was excited at 458 nm (fluorescence emission: 465–550 nm), GFP and BCECF at 488 nm (fluorescence emission: 500–550 nm), YFP at 514 nm (fluorescence emission: 525–578 nm), and FM4-64 and PI at 561 nm (fluorescence emission 599–680 for FM4-64 and 644–753 nm for PI). Whenever vacuolar morphology was analyzed, roots were mounted in PI solution (0.02 mg/mL) to counterstain cell walls. MDY-64, FM4-64, and BCECF staining was performed as described previously (32). Z-stacks were recorded with a step size of 420 nm, resulting in 25–35 Z-stack images per cell. The 3D surface renderings, using vacuoles loaded with BCECF-AM, were achieved using the ImageJ plug-in 3-D Viewer (rsb.info.nih.gov/ij/). We used MorphoGraphX (33) to segment 3D cell boundaries (based on PI signal), allowing us to depict the cell volume in relation to vacuolar volume (based on the BCECF signal). Imaging and rendering settings were constant within an experiment.

FRAP Measurements. For FRAP measurements, a Leica TCS SP5II microscope equipped with an HCX PL APO lambda blue 63.0 × 1.20 WATER UV water-immersion objective was used. *Arabidopsis* seedlings (5 d after germination) were incubated for 18 h in liquid 1/2 MS medium supplemented with 250 nM NAA or the corresponding volume of DMSO. At 15 h into incubation, membrane-permeant BCECF-AM (10 μM) (Molecular Probes; Invitrogen) was added for 2 h. The seedlings then were washed for 1 h in their respective solution without BCECF and were imaged afterward. FRAP experiments were carried out with the FRAP Wizard implemented in the Leica LAS AF software. The area of interest was selected and bleached using the "Bleach Point" mode. All experiments consisted of four prebleach frames, a point bleach step for 250 ms with a laser power between 30% and 50%, and 40–50 subsequent frames of postbleach acquisition. Image acquisition was performed at a scanning speed of 1,400 Hz (bidirectional scanning), a resolution of 512 × 512 pixels at a zoom-factor of 6 (pixel size 80.2 nm × 80.2 nm), and a line-average of 3. BCECF was excited at 488 nm, and its emission was detected with a Hybrid detector (standard mode) between 495 and 560 nm. The bleach point area was used to measure FRAP. Recovery halftime was calculated with the FRAP Profiler plug-in for ImageJ. The boxplots were generated with OriginPro 2015 (OriginLab).

Superresolution Microscopy. For image acquisition, an inverted Leica SP8 (DMi8) microscope, equipped with a gSTED module, operating with a depletion laser at a wavelength of 592 nm, was used. For excitation of Lifeact–Venus, a pulsed supercontinuum laser (white light laser; WLL II) was used at 510 nm. Emission fluorescence was detected with a HyD detector at 525–578 nm). The Leica HC PL APO CS2 100 × 1.4 objective was used. Pixel dwell time was between 500 nm and 1 μm. To quantify auxin-mediated changes of the cytoskeleton organization, we measured the skewness of Lifeact–Venus-marked actin filaments. For that measurement, z-stacks (step size 0.42 μm, 25–35 sections per stack) of entire meristematic cells were acquired and subsequently were processed with

ImageJ (rsb.info.nih.gov/ij/). All z-stack images were skeletonized and projected, and the skewness of the actin filaments, indicating the degree of actin bundling, was measured as described previously (14).

SEM. *Arabidopsis* seedlings roots were cut off and submerged in fixative (1% paraformaldehyde, 1% glutaraldehyde, 2% sucrose, and 2 mM CaCl in 0.1 M NaCac buffer) for 1 h at room temperature, processed using the zinc iodide osmium impregnation technique, and embedded in Spurr resin (44). Root tips then were mounted onto 3View stubs (Gatan) with conductive epoxy (Chemtronics) and were hardened for 4 h at 100 °C. The final trimmed block was sputtercoated with gold for 30 s (layer thickness ∼20 nm) to improve conductivity. SBF-SEM images were collected on a Merlin Compact scanning electron microscope (Zeiss) with the Gatan 3View system. Section thickness was set to 100 nm, and the block face was imaged in variable pressure mode (∼50 Pa) at 4 kV acceleration voltage with a pixel dwell time of 7–8 μs and pixel size of 0.009 μm (*Col-0*) or 0.015 μm (*Col-0*+NAA). Data processing (stack formation, image alignment, and trimming and scaling of sections to a common mean and SD) was done in the imod software package (45). The Amira software (FEI) magic wand tool was used to select the vacuoles throughout the entire cell. Areas with zinc iodide osmium deposits in the vacuoles that blocked selection by the magic wand tool were added to the material manually by using the brush tool. The contours were smoothed twice with a filter mask size 5. The 3D model was visualized using surface generation and surface view.

Analysis and Data Presentation. All experiments were carried out at least three times. Replicates were biological replicates from different plants. All figures show representative experiments, and the sample size for each experiment is given in the figure legends. Data are shown as mean ± SEM. Statistical significance was evaluated by the Student's *t*-test using GraphPad (www.graphpad.com/quickcalcs/).

ACKNOWLEDGMENTS. We thank Valerian Dolja, Elison B. Blancaflor, Richard J. Cyr, Nico Geldner, Takashi Ueda, Ken-ichiro Hayashi, Erik Nielson, Masao Tasaka, and Richard B. Meagher for providing published research tools; the University of Natural Resources and Life Sciences-Vienna Institute of BioTechnology Imaging Centre for access and expertise; David Whittaker for help with the manuscript; and Elsa Arcalis for technical support and advice. This work was supported by the Vienna Science and Technology Fund (Vienna Research Group); by Grants P26568-B16 and P26591-B16 from the Austrian Science Fund; by European Research Council Starting Grant 639478-AuxinER (to J.K.-V.); and by Deutsche Forschungsgemeinschaft Personal Postdoctoral Fellowships (to D.S. and C.L.). The Biotechnology and Biological Sciences Research Council provided Advanced Life Sciences Research Technology Initiative 13 funding for SBF-SEM through Grant BB/C014122/1 (to C.H.).

1. Fletcher DA, Mullins RD (2010) Cell mechanics and the cytoskeleton. *Nature* 463(7280): 485–492.
2. Faix J, et al. (1996) Cortexillins, major determinants of cell shape and size, are actin-bundling proteins with a parallel coiled-coil tail. *Cell* 86(4):631–642.
3. Thomas C, Staiger CJ (2014) A dynamic interplay between membranes and the cytoskeleton critical for cell development and signaling. *Front Plant Sci* 5:335.
4. Sauer M, Robert S, Kleine-Vehn J (2013) Auxin: Simply complicated. *J Exp Bot* 64(9): 2565–2577.
5. Rahman A, et al. (2007) Auxin, actin and growth of the Arabidopsis thaliana primary root. *Plant J* 50(3):514–528.
6. Dhonukshe P, et al. (2008) Auxin transport inhibitors impair vesicle motility and actin cytoskeleton dynamics in diverse eukaryotes. *Proc Natl Acad Sci USA* 105(11):4489–4494.
7. Nick P, Han MJ, An G (2009) Auxin stimulates its own transport by shaping actin filaments. *Plant Physiol* 151(1):155–167.
8. Nagawa S, et al. (2012) ROP GTPase-dependent actin microfilaments promote PIN1 polarization by localized inhibition of clathrin-dependent endocytosis. *PLoS Biol* 10(4):e1001299.
9. Lanza M, et al. (2012) Role of actin cytoskeleton in brassinosteroid signaling and in its integration with the auxin response in plants. *Dev Cell* 22(6):1275–1285.
10. Li G, et al. (2014) Rice actin-binding protein RMD is a key link in the auxin-actin regulatory loop that controls cell growth. *Proc Natl Acad Sci USA* 111(28):10377–10382.
11. Zhu J, Geisler M (2015) Keeping it all together: Auxin-actin crosstalk in plant development. *J Exp Bot* 66(16):4983–4998.
12. Riedl J, et al. (2008) Lifeact: A versatile marker to visualize F-actin. *Nat Methods* 5(7): 605–607.
13. Hayashi K, et al. (2012) Rational design of an auxin antagonist of the SCF(TIR1) auxin receptor complex. *ACS Chem Biol* 7(3):590–598.
14. Higaki T, Kutsuna N, Sano T, Kondo N, Hasezawa S (2010) Quantification and cluster analysis of actin cytoskeletal structures in plant cells: Role of actin bundling in stomatal movement during diurnal cycles in Arabidopsis guard cells. *Plant J* 61(1):156–165.
15. Löfke C, Dünser K, Scheuring D, Kleine-Vehn J (2015) Auxin regulates SNARE-dependent vacuolar morphology restricting cell size. *eLife* 4:e05868.
16. Mathur J, Mathur N, Kernebeck B, Hülskamp M (2003) Mutations in actin-related proteins 2 and 3 affect cell shape development in Arabidopsis. *Plant Cell* 15(7):1632–1645.
17. Carter C, et al. (2004) The vegetative vacuole proteome of Arabidopsis thaliana reveals predicted and unexpected proteins. *Plant Cell* 16(12):3285–3303.
18. Li J, et al. (2012) Capping protein modulates the dynamic behavior of actin filaments in response to phosphatidic acid in Arabidopsis. *Plant Cell* 24(9):3742–3754.
19. Staiger CJ, et al. (1994) Microinjected profilin affects cytoplasmic streaming in plant cells by rapidly depolymerizing actin microfilaments. *Curr Biol* 4(3):215–219.
20. Gilliland LU, Pawloski LC, Kandasamy MK, Meagher RB (2003) Arabidopsis actin gene ACT7 plays an essential role in germination and root growth. *Plant J* 33(2):319–328.
21. Kandasamy MK, McKinney EC, Meagher RB (2009) A single vegetative actin isovariant overexpressed under the control of multiple regulatory sequences is sufficient for normal Arabidopsis development. *Plant Cell* 21(3):701–718.
22. Peremyslov VV, Prokhnevsky AI, Dolja VV (2010) Class XI myosins are required for development, cell expansion, and F-Actin organization in Arabidopsis. *Plant Cell* 22(6):1883–1897.
23. Nováková P, et al. (2014) SAC phosphoinositide phosphatases at the tonoplast mediate vacuolar function in Arabidopsis. *Proc Natl Acad Sci USA* 111(7):2818–2823.
24. Cui Y, et al. (2014) Activation of the Rab7 GTPase by the MON1-CCZ1 Complex Is Essential for PVC-to-Vacuole Trafficking and Plant Growth in Arabidopsis. *Plant Cell* 26(5):2080–2097.
25. Zheng J, Han SW, Rodriguez-Welsh MF, Rojas-Pierce M (2014) Homotypic vacuole fusion requires VTI11 and is regulated by phosphoinositides. *Mol Plant* 7(6):1026–1040.
26. Mitsuhashi N, Shimada T, Mano S, Nishimura M, Hara-Nishimura I (2000) Characterization of organelles in the vacuolar-sorting pathway by visualization with GFP in tobacco BY-2 cells. *Plant Cell Physiol* 41(9):993–1001.
27. Gao XQ, et al. (2005) The dynamic changes of tonoplasts in guard cells are important for stomatal movement in Vicia faba. *Plant Physiol* 139(3):1207–1216.
28. Reisen D, Marty F, Leborgne-Castel N (2005) New insights into the tonoplast architecture of plant vacuoles and vacuolar dynamics during osmotic stress. *BMC Plant Biol* 5:13–25.
29. Ruthardt N, Gulde N, Spiegel H, Fischer R, Emans N (2005) Four-dimensional imaging of transvacuolar strand dynamics in tobacco BY-2 cells. *Protoplasma* 225(3-4):205–215.
30. Tanaka Y, et al. (2007) Intra-vacuolar reserves of membranes during stomatal closure: The possible role of guard cell vacuoles estimated by 3-D reconstruction. *Plant Cell Physiol* 48(8):1159–1169.
31. Viotti C, et al. (2013) The endoplasmic reticulum is the main membrane source for biogenesis of the lytic vacuole in Arabidopsis. *Plant Cell* 25(9):3434–3449.
32. Scheuring D, Schöller M, Kleine-Vehn J, Löfke C (2015) Vacuolar staining methods in plant cells. *Methods Mol Biol* 1242:83–92.
33. Barbier de Reuille P, et al. (2015) MorphoGraphX: A platform for quantifying morphogenesis in 4D. *eLife* 4:05864.
34. Fujiwara M, et al. (2014) Interactomics of Qa-SNARE in Arabidopsis thaliana. *Plant Cell Physiol* 55(4):781–789.
35. Owens T, Poole RJ (1979) Regulation of cytoplasmic and vacuolar volumes by plant cells in suspension culture. *Plant Physiol* 64(5):900–904.
36. Docampo R, Jimenez V, Lander N, Li ZH, Niyogi S (2013) New insights into roles of acidocalcisomes and contractile vacuole complex in osmoregulation in protists. *Int Rev Cell Mol Biol* 305:69–113.
37. Era A, et al. (2009) Application of Lifeact reveals F-actin dynamics in Arabidopsis thaliana and the liverwort, Marchantia polymorpha. *Plant Cell Physiol* 50(6):1041–1048.
38. Sheahan MB, Rose RJ, McCurdy DW (2004) Organelle inheritance in plant cell division: The actin cytoskeleton is required for unbiased inheritance of chloroplasts, mitochondria and endoplasmic reticulum in dividing protoplasts. *Plant J* 37(3):379–390.
39. Wang YS, Motes CM, Mohamalawari DR, Blancaflor EB (2004) Green fluorescent protein fusions to Arabidopsis fimbrin 1 for spatio-temporal imaging of F-actin dynamics in roots. *Cell Motil Cytoskeleton* 59(2):79–93.
40. Marc J, et al. (1998) A GFP-MAP4 reporter gene for visualizing cortical microtubule rearrangements in living epidermal cells. *Plant Cell* 10(11):1927–1940.
41. Geldner N, et al. (2009) Rapid, combinatorial analysis of membrane compartments in intact plants with a multicolor marker set. *Plant J* 59(1):169–178.
42. Preuss ML, et al. (2006) A role for the RabA4b effector protein PI-4Kbeta1 in polarized expansion of root hair cells in Arabidopsis thaliana. *J Cell Biol* 172(7):991–998.
43. Yano D, et al. (2003) A SNARE complex containing SGR3/AtVAM3 and ZIG/VTI11 in gravity-sensing cells is important for Arabidopsis shoot gravitropism. *Proc Natl Acad Sci USA* 100(14):8589–8594.
44. Hawes CR, Juniper BE, Horne JC (1981) Low and high voltage electron microscopy of mitosis and cytokinesis in maize roots. *Planta* 152(5):397–407.
45. Kremer JR, Mastronarde DN, McIntosh JR (1996) Computer visualization of three-dimensional image data using IMOD. *J Struct Biol* 116(1):71–76.